Science Advances
AAAS

Supplementary Materials for

Distinguishing surface and bulk electromagnetism via their dynamics in an intrinsic magnetic topological insulator

Khanh Duy Nguyen *et al.*

Corresponding author: Shuolong Yang, yangsl@uchicago.edu

Sci. Adv. **10**, eadn5696 (2024)
DOI: 10.1126/sciadv.adn5696

This PDF file includes:

Supplementary Text S1 to S7
Figs. S1 to S11
References

Supplementary Text

1. Modified Fermi Dirac Fitting

The ARPES spectra are integrated around $\bar{\Gamma}$ in the momentum window of [-0.2, +0.2] Å^{-1}. The resulting energy distribution curves (EDCs) are fitted to the modified Fermi-Dirac (FD) profile on the log scale to make sure the data points at energies (ε) far above the Fermi level are weighted properly. Based on the original FD function for the free electron gas with a chemical potential at μ:

$$n(\epsilon, T) = \frac{1}{e^{\epsilon-\mu/k_B T} + 1}, \qquad (s1.1)$$

where $k_B T$ is the thermal energy, we used the following function for fitting:

$$f(\epsilon, T) = \ln\left[\left(\frac{A + B\epsilon}{1 + e^{\epsilon-\mu/k_B T}} + F\right) \otimes \mathrm{Gauss}(\epsilon, \Delta\epsilon)\right] + f_0(\mu, C, D). \qquad (s1.2)$$

Here, first we convolve the FD function with the Gaussian distribution function, Gauss(ε,$\Delta\varepsilon$) where the energy resolution $\Delta\varepsilon$ corresponds to the full width half maximum (FWHM) of the Gaussian function. We approximate the DOS near μ using a linear function $A + B\varepsilon$. F is the background intensity. $f_0(\mu,C,D)$ is the background function on a log scale, which is comprised of a constant background for $\epsilon < \mu$ joint with a linearly decaying profile for $\varepsilon > \mu$, in the form of $C + D\varepsilon$. This empirical function accounts for the background signals from different sources including instrument artifacts, non-thermalized hot electrons, excitation continuum, etc., which are normally negligible on the linear scale. This background has a minimal impact on the FD fitting after 360 fs due to the thermalized electronic distribution, which is what the main text focuses on.

The parameters for fitting are:

- A, B: parameters for the DOS function near μ,
- F: background on the linear scale,
- C, D: parameters for the background function at $\varepsilon > \mu$ on the logarithmic scale,
- μ: chemical potential,
- ***T*: electronic temperature**.

The energy resolution $\Delta\varepsilon = 20$ meV is obtained by fitting EDCs obtained from static ARPES at 12K with the same probe. The fitting function for this case is simply:

$$f'(\epsilon) = \left(\frac{A + B\epsilon}{1 + e^{\epsilon-\mu}/_{k_B T}} + F\right)_{T=12\ \mathrm{K}} \otimes \mathrm{Gauss}(\epsilon, \Delta\epsilon). \qquad (s1.3)$$

The fitting results using the modified FD profile are shown in Fig. S1 for two IR fluences at 10 and 20 μJ/cm^2 at some representative delays. Note that the modified FD fitting was done on a large number of delay points, whereas the detailed exchange gap analysis in main text Fig. 2 could only be performed on extremely high-quality ARPES spectra taken separately at a small subset of delay points.

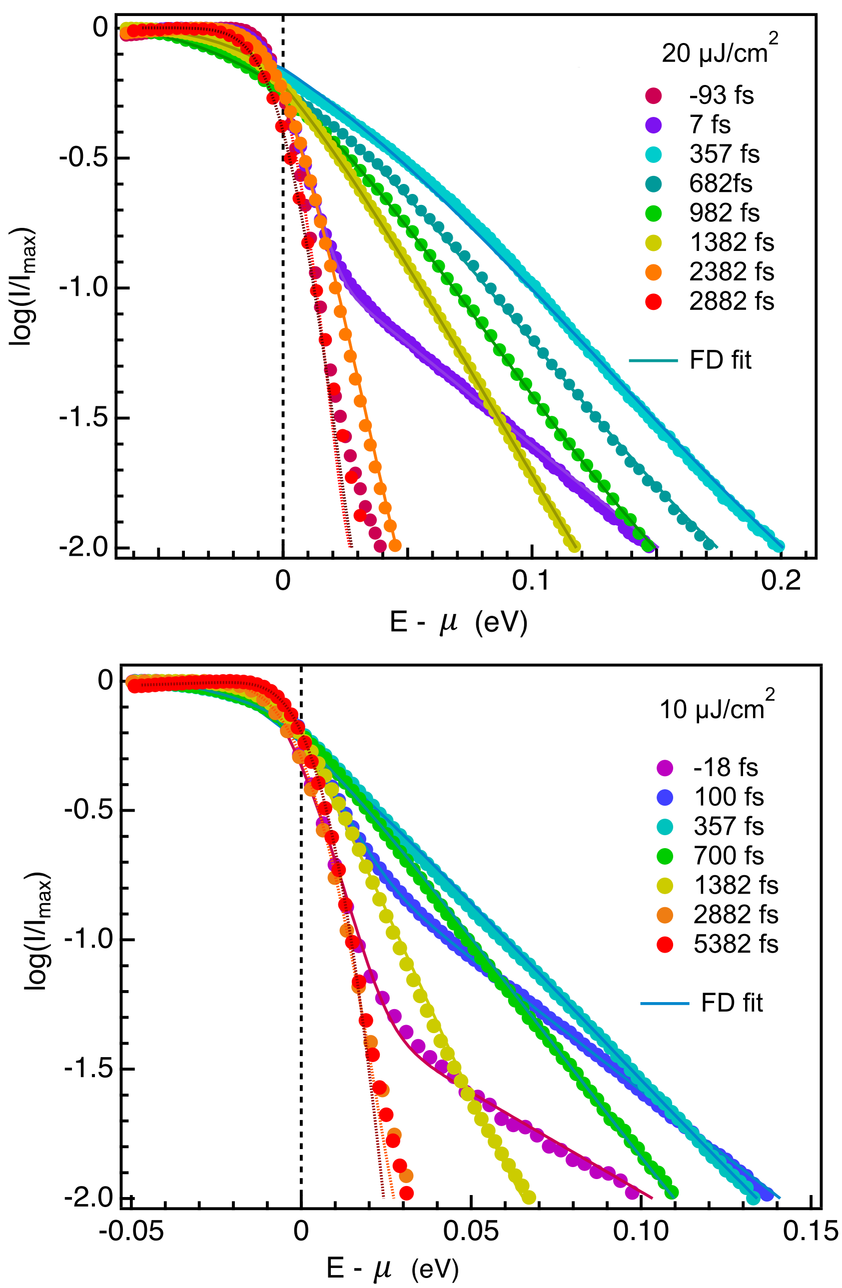

Fig. S1. Modified-FD fitting results for representative delays at incident IR fluences of 10 and 20 μJ/cm².

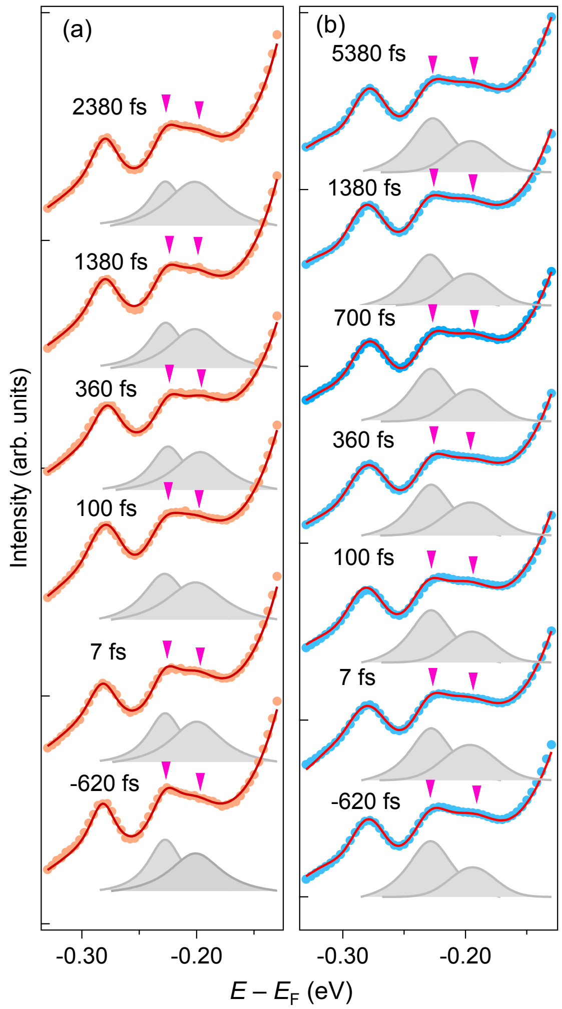

Fig. S2. Five-Lorentzian-peak fitting results for sub-bands S_1 and S_2 at representative delays. Only the two peaks corresponding to the *q*-2DSs are shown in the figure. (a) The results for the IR pump fluence of 20 μJ/cm^2. (b) The results for the IR pump fluence of 20 μJ/cm^2.

2. Microscopic Boltzmann Transport Model

TrARPES yields the time dependence of electronic structures. In the following, we perform calculations to estimate the ultrafast dynamics of bosonic quasiparticle ensembles (phonons and magnons) to facilitate the subsequent discussion on the demagnetization mechanisms (Supplementary Text 6). We follow the Boltzmann transport formalism, take into account electron-boson couplings (*77*, *78*), and assume that the electron population is instantaneously thermalized at any time point (*79*).

Assuming Bose-Einstein (BE) statistics for phonons and magnons, we have:

$$\left(\frac{\partial f(E_k)}{\partial t}\right)_{e-b} = -\frac{2\pi}{\hbar}\sum_{k,\eta}|g(\boldsymbol{k},\boldsymbol{k}';\eta)|^2\{f(E_k)[1-f(E_{k'})]n(\boldsymbol{q},\eta)\delta\big(E_k-E_{k'}+\hbar\omega(\boldsymbol{q},\eta)\big)$$
$$+f(E_{\boldsymbol{k}})[1-f(E_{k'})][1+n(\boldsymbol{q},\eta)]\delta\big(E_k-E_{k'}-\hbar\omega(\boldsymbol{q},\eta)\big)$$
$$-f(E_{\boldsymbol{k}'})[1-f(E_k)][1+n(\boldsymbol{q},\eta)]\delta\big(E_k-E_{k'}+\hbar\omega(\boldsymbol{q},\eta)\big)$$
$$-f(E_{\boldsymbol{k}'})[1-f(E_k)][n(\boldsymbol{q},\eta)]\delta\big(E_k-E_{k'}-\hbar\omega(\boldsymbol{q},\eta)\big)\}. \qquad (s2.1)$$

Here, $f(E_k)$ is the occupation function of electrons at energy E_k. At equilibrium, this function is the Fermi-Dirac function. The bosonic distribution, $n(\boldsymbol{q},\eta)$ follows:

$$\left(\frac{\partial n(E_k)}{\partial t}\right)_{e-b} = -\frac{4\pi}{\hbar}\sum_{k}|g(\boldsymbol{k},\boldsymbol{k}';\eta)|^2 f(E_k)[1-f(E_{k'})]\,\big[n(\boldsymbol{q},\eta)\delta\big(E_k-E_{k'}+\hbar\omega(\boldsymbol{q},\eta)\big)$$
$$-[1+n(\boldsymbol{q},\eta)]\delta\big(E_k-E_{k'}-\hbar\omega(\boldsymbol{q},\eta)\big)\big]. \qquad (s2.2)$$

These equations consider 4 processes involving an electron at momentum state $\boldsymbol{k}$ being scattered to a new state of momentum $\boldsymbol{k}'$, accompanied by generating or annihilating a boson of energy $\hbar\omega(\boldsymbol{q},\eta)$, where $\boldsymbol{q}$ and η are momentum and polarization (or mode) of that boson, respectively. $g(\boldsymbol{k},\boldsymbol{k}';\eta)$ is the coupling strength. Based on the Éliashberg model for electron-boson coupling, the Éliashberg coupling function $\alpha^2F(\omega)$, $F(\omega)$ being the density of states (DOS) for the bosons) and electron-boson coupling constant (λ_{e-b}) can be derived as (*78*):

$$\alpha^2F(\omega) = N(E_F)\sum_{\eta}\int\frac{d\Omega_{\boldsymbol{k}}}{4\pi}\int\frac{d\Omega_{\boldsymbol{k}'}}{4\pi}|g(\boldsymbol{k},\boldsymbol{k}';\eta)|^2\delta\big(\hbar\omega-\hbar\omega(\boldsymbol{q},\eta)\big), \qquad (s2.3)$$

$$\lambda_{e-b} = 2\int_0^{\omega_{max}}\frac{\alpha^2F(\omega)}{\omega}d\omega. \qquad (s2.4)$$

If we further approximate that $g(\boldsymbol{k},\boldsymbol{k}';\eta)$ is isotropic, then $\alpha^2F(\omega)$ is directly proportional to $|g(\boldsymbol{k},\boldsymbol{k}';\eta)|^2$and λ_{e-b} can be easily obtained.

We apply this framework to our case with the following considerations: (1) Transient electronic temperatures are obtained by the modified FD fitting described in Supplementary Text 1. (2) For phonons, the phonon DOS (phDOS) is taken from Ref.(*80*); while for magnons, the magnon DOS (mDOS) was measured in a neutron scattering study (*81*). (3) Using the equation for the heat capacities of phonons and magnons (Eqn. (s2.5)) and the calculated ratio of these two from a previous DFT calculation (*80*), we deduce the ratio between the amplitudes of phDOS and mDOS.

$$c_v = \frac{dU}{dT} = \sum_{\eta} d\omega D_\eta(\omega) \frac{\frac{(\hbar\omega)^2}{k_B T} e^{\beta\hbar\omega}}{(e^{\beta\hbar\omega} - 1)^2}. \qquad (s2.5)$$

(4) The electronic density of states (eDOS) is taken from Ref.(*80*). (5) The evolution of $f\,(E_k)$ is then numerically calculated by (s2.1) and (s2.2) which yield transient electronic temperatures. At time zero, the electron population is suddenly changed to an FD distribution with an elevated temperature; then it is relaxed via scattering with phonons and magnons. The phonon and magnon populations are forced to follow the BE distribution at any given time and decay according to their own decay rates: $dT_b/dt = -(T_b - 12\text{ K})/\tau_b$,which roughly approximate the bosonic decays due to boson-boson interactions and diffusions. The electron population is enforced to follow the FD distribution at any given time. Also, since the model assumes all particle ensembles are thermalized, we force T_m to stay under $T_N \sim 25$ K, which allows long range magnetic order to exist. The calculated evolution of the electronic temperature then serves as a fitting function for the experimental data. Overall, the fitting parameters in this calculation are the decay rate of the phonon temperature (τ_b), the decay rate of the magnon temperature (τ_m), scaling factor for phDOS (and mDOS) as compared to eDOS, and the Éliashberg coupling strength α^2. Finally, the calculation results in $\lambda_{e\text{-}ph} \approx 0.2$ and a minimal contribution from magnons ($\lambda_{e\text{-}m} < 0.01$). Note that the small electron-magnon coupling strength only represents the coupling with low-frequency magnons, with the static magnetization being the zero-frequency component. The overall electron-magnon coupling can be much larger.

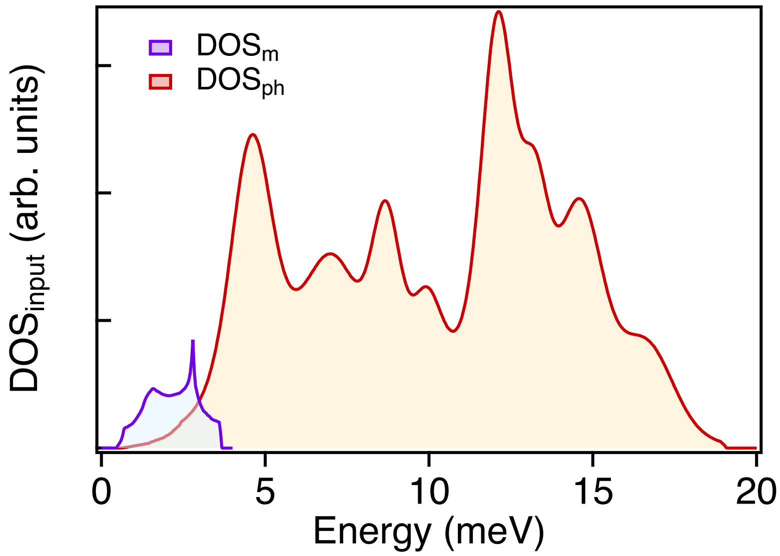

Fig. S3. Density of states (DOS) functions for phonons and magnons and their relative scaling.

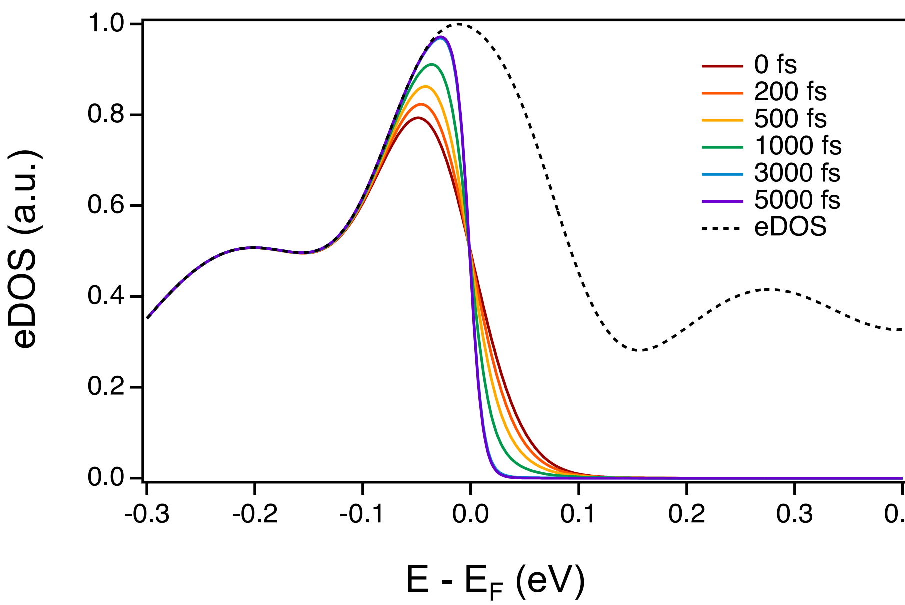

Fig. S4. Electronic DOS function of MBT (dashed line) multiplied with FD functions (solid lines) and its evolution in the numerical calculation.

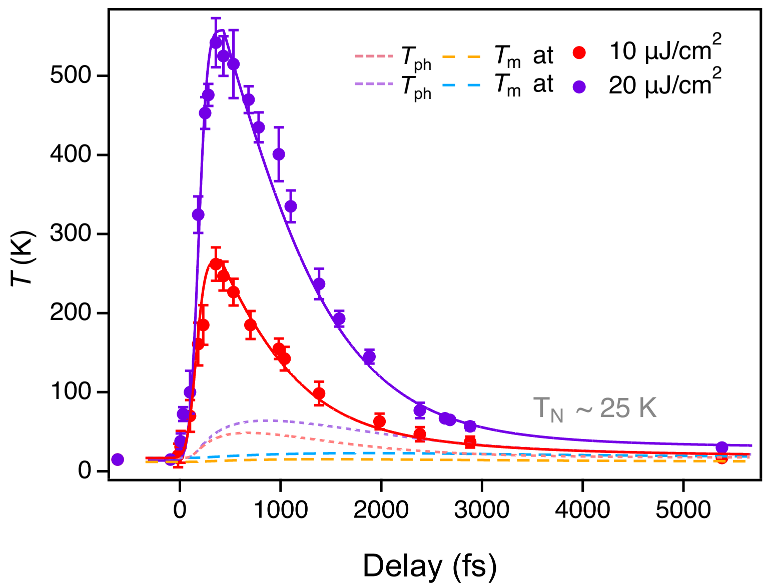

Fig. S5. Microscopic Boltzmann transport simulation and fitting of electronic temperatures for MBT. The solid lines are the fitting curves for the experimental transient electronic temperatures using two fluences. The purple and red dashed lines are the corresponding phonon temperatures. The blue and yellow dashed lines correspond to the resulted magnon temperatures.

3. Electronic Temperature Dynamics in the MBT/BT Heterostructure

We performed control experiments on $MnBi_2Te_4/(Bi_2Te_3)_{30}$ [MBT/(BT)$_{30}$] and (BT)$_{27}$ films, grown by molecular beam epitaxy (Methods), using trARPES (Fig. S6(a)). These films' quality was optimized such that the electronic and structural properties are comparable to the single crystals. By the same procedure described in Supplementary Text 1, we extract the electronic temperature T_e and the electronic relaxation time scale using $\tau = -T_e/(dT_e/dt)$ near the maximum T_e. The relaxation time scales are similar for bulk-crystal MBT and MBT/(BT)$_{30}$ films, being ~ 1 ps and ~ 1.6 ps, respectively, despite the different species of materials underneath the top MBT layer. In contrast, the time scale for the (BT)$_{27}$ film is ~6 ps (Fig. S6(b)). Moreover, the maximum T_e's reached by bulk-crystal MBT and MBT/(BT)$_{30}$ film are both in the range of 260-270 K using the pump fluence of ~10 $\mu J/cm^2$ (Fig. S6(b)). This comparison suggests that the electronic relaxation dynamics in MBT is mostly unaffected by scattering processes in the layers underneath the top MBT layer, or by diffusion along the *c*-axis. Correspondingly, the wavefunctions of the electronic states near E_F in bulk-crystal MBT and MBT/(BT)$_{30}$ cannot have substantial presence in the layers underneath the top MBT layer. The long-lived excited population in Bi_2Te_3 is attributed to the bulk-to-surface scattering which continues to refill the topological surface state using electrons from the bulk conduction band reservoir(*82*).

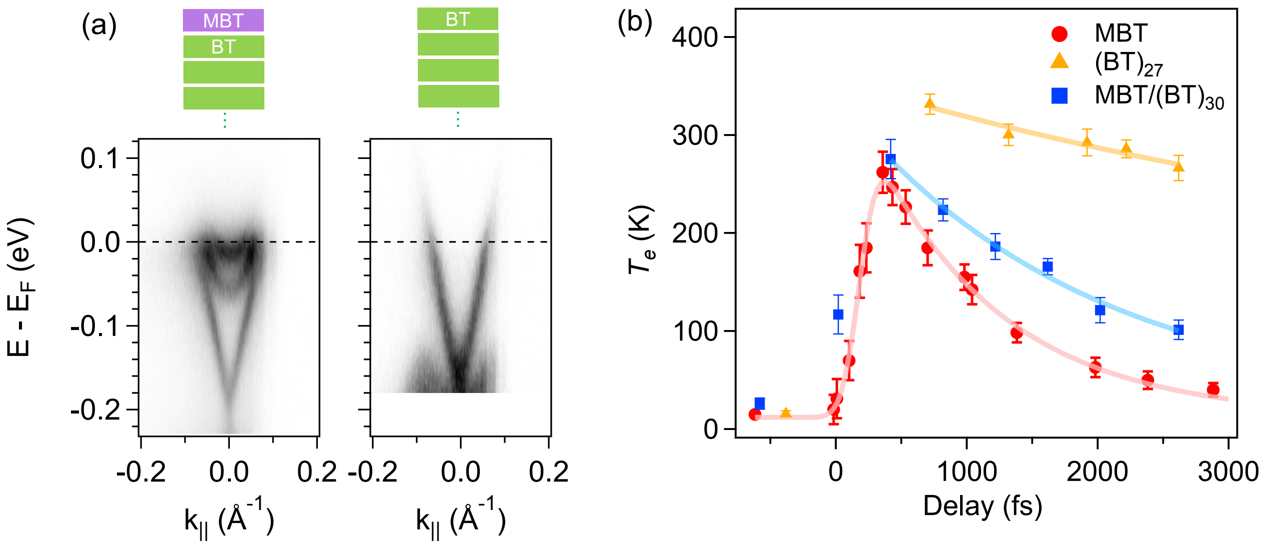

Fig. S6. Comparison between the T_e dynamics of the MBT single crystal, MBT/(BT)$_{30}$ heterostructure, and (BT)$_{27}$ film. The latter two are grown by molecular beam epitaxy (MBE). (a) trARPES spectra of the MBT/(BT)$_{30}$ (left) and (BT)$_{27}$ film (right) taken at ~500 fs. (b) The T_e dynamics of the three systems, MBT and MBT/(BT)$_{30}$ have similar relaxation dynamics, in contrast with the case of the (BT)$_{27}$ film. Error bars show one standard deviation of the fitting uncertainties.

4. 2D RKKY Model

We start from the Kondo lattice model. The Hamiltonian is:

$$H_{\mathrm{KL}} = \sum_{\boldsymbol{k},\sigma} \varepsilon_{\boldsymbol{k}} \hat{c}^{\dagger}_{\boldsymbol{k},\sigma} \hat{c}_{\boldsymbol{k},\sigma} + J \sum_{i} \boldsymbol{S}_i \cdot \boldsymbol{s}_i. \qquad \text{(s4.1)}$$

The second term corresponds to the coupling between the localized spin $\boldsymbol{S}_i$ and the effective spin of the conduction electrons $\boldsymbol{s}_i$. J is the Kondo coupling constant. In a Kondo lattice, there are two scenarios for the ground state of the system as indicated by the Doniach phase diagram: a Fermi liquid of Kondo singlets or a cooperative magnetic system, known as the RKKY picture (*45*). The RKKY interaction is derived from Eqn. (s4.1) by reducing the Hamiltonian to the space of the localized spins $\boldsymbol{S}_i$:

$$\sum_{i\neq j} \langle \boldsymbol{S}_i | H_{KL} | \boldsymbol{S}_j \rangle \longrightarrow H_{\mathrm{RKKY}} = \sum_{\boldsymbol{k},\sigma} \varepsilon'_{\boldsymbol{k}} \hat{c}^{\dagger}_{\boldsymbol{k},\sigma} \hat{c}_{\boldsymbol{k},\sigma} + \frac{1}{2} \sum_{i\neq j} \mathfrak{J}_{ij} \boldsymbol{S}_i \cdot \boldsymbol{S}_j. \qquad \text{(s4.2)}$$

Here, $\mathfrak{J}_{ij}$ is the RKKY coupling constant; $\varepsilon'_{\boldsymbol{k}}$ indicates the kinetic energy after the transformation and is different from the first term on the RHS of Eqn. (s4.1). $\mathfrak{J}_{ij}$ is formulated as:

$$\mathfrak{J}_{ij} = -\left(\frac{J}{N}\right)^2 \sum_{\boldsymbol{k},\boldsymbol{q}} \cos\left[(\boldsymbol{k}-\boldsymbol{q})\cdot(\boldsymbol{r}_i - \boldsymbol{r}_j)\right] \frac{n_{\boldsymbol{k}} - n_{\boldsymbol{q}}}{\varepsilon_{\boldsymbol{q}} - \varepsilon_{\boldsymbol{k}}}, \qquad \text{(s4.3)}$$

or in the continuous limit

$$\mathfrak{J}_{ij} = -2\left(\frac{J}{NV}\right)^2 \iint d\boldsymbol{k} d\boldsymbol{q} \cos\left[(\boldsymbol{k}-\boldsymbol{q})\cdot \boldsymbol{R}_{ij}\right] \frac{n_{\boldsymbol{k}}}{\varepsilon_{\boldsymbol{q}} - \varepsilon_{\boldsymbol{k}}}, \qquad \text{(s4.4)}$$

where, $\boldsymbol{R}_{ij} \equiv \boldsymbol{r}_i - \boldsymbol{r}_j$; V is the total volume in the momentum space. We can remove the $n_{\boldsymbol{q}}$ term in (s4.3) due to the symmetry between $\boldsymbol{k}$ and $\boldsymbol{q}$ in this formalism. Now we calculate the RKKY coupling constant in 2D. Eqn. (s4.4) in 2D polar coordinates becomes:

$$\mathfrak{J}_{ij} = -2\left(\frac{J}{NV}\right)^2 \iint_0^{\infty} kq dk dq \iint_0^{2\pi} d\theta_k \, d\theta_q \cos\left[kR_{ij}\cos\theta_k - qR_{ij}\cos\theta_q\right] \frac{n_{\boldsymbol{k}}}{\varepsilon_{\boldsymbol{q}} - \varepsilon_{\boldsymbol{k}}}. \qquad \text{(s4.5)}$$

Solving this integral yields the following results, with $J_0(x)$ and $Y_0(x)$ being the zero-order Bessel functions of the first and second kinds, respectively:

$$\begin{aligned}
\Im_{ij} &= -2\left(\frac{2\pi J}{NV}\right)^2 \iint_0^\infty kqdkdq\, J_0(kR_{ij})J_0(qR_{ij})\frac{n_k}{\varepsilon_q-\varepsilon_k} \\
&= -2\left(\frac{2\pi J}{NV}\right)^2 \frac{2m}{\hbar^2}\int_0^\infty dkk\, J_0(kR_{ij})n_k \int_0^\infty dq\,\frac{qJ_0(qR_{ij})}{q^2-k^2} \\
&= \left(\frac{2\pi J}{NV}\right)^2 \frac{2m\pi}{\hbar^2}\int_0^\infty dkk\, J_0(kR_{ij})Y_0(kR_{ij})n_k(T). \qquad (s4.6)
\end{aligned}$$

Combined with the temperature dependence of the Kondo coupling constant, the total temperature dependency of the RKKY coupling strength finally becomes

$$J_{\mathrm{RKKY}} = \sum_{i\neq j}\left(\frac{2\pi J(T)}{NV}\right)^2 \frac{2m\pi}{\hbar^2}\int_0^\infty dkk\, J_0(kR_{ij})Y_0(kR_{ij})n_k(T). \qquad (s4.7)$$

The Anderson's Poor-Man scaling renormalization reduces the energy range of excitations in the Kondo model to the conduction band only. It is valid as long as the electronic temperature is larger than the Kondo temperature. Therefore, in our study of MBT, considering $T > 12$ K and that MBT is a cooperative magnetic system, this scaling approach should be appropriate. The value of ρJ in Eqn. (3) of the main text is calculated as (*43*):

$$J\rho = \frac{4\Delta}{\pi U} \qquad (s4.8)$$

in which, Δ is the so-called bare resonant level width of the Anderson model which is approximately the spectral half-width of the localized band; U is the repulsive potential of 3*d* electrons.

Specifically, we gather the following details of the band structure for the calculation of J_{pd} using this model:

- Mn 3*d* flat band localized at -4 eV with a spectral FWHM ~ 0.4 eV (*40*), thus Δ ~ 0.2 eV,
- Assuming $U = 2E_B^{3d}$ ~ 8 eV,
- Conduction band bottom at -0.25 eV (we assume the Fermi level crossing in the middle of the band), thus D = 0.25 eV and the corresponding temperature is ~2900 K,
- The RKKY interaction becoming negligible beyond 10 unit-cell distances from a Mn atom, thus we only sum until 10 unit-cells in equation (s4.7). The absolute value of this RKKY interaction strength is negative, supporting the ferromagnetic ground state for the top septuple layer of MBT.

5. RKKY Coupling Strength and Magnetization

We use the Weiss model of ferromagnetism to relate the change in the RKKY coupling constant to the change in magnetization. Magnetization at a finite temperature can be found by solving simultaneously the two following equations (*83*):

$$\begin{cases} \dfrac{M}{M_s} = B_j(y) & \text{(s5.1)} \\ y = \dfrac{g_j \mu_B j \lambda M}{k_B T}, & \text{(s5.2)} \end{cases}$$

where M and M_s are the magnetization and its saturation value, respectively; $B_j(y)$ is the Brillouin function; j is the spin number; g_j is the Landé-g value; μ_B is the Bohr magneton; λ is a constant parameterizing the strength of the molecular field as a function of the magnetization:

$$\lambda = -\frac{2V}{(g\mu_B)^2}\frac{\sum_j J_{ij}\boldsymbol{S_j}}{\sum_j \boldsymbol{S_j}}. \qquad \text{(s5.3)}$$

The Curie temperature can also be written as:

$$T_C = \frac{g_j \mu_B (j+1)\lambda M_s}{3k_B}. \qquad \text{(s5.4)}$$

Therefore, equation (s5.2) becomes

$$\frac{M}{M_s} = \frac{k_B T y}{g_j \mu_B j} \cdot \frac{g_j \mu_B (j+1)}{3k_B T_C} = \frac{(j+1)Ty}{3jT_C}. \qquad \text{(s5.5)}$$

Eventually, solving (s5.1) and (s5.2) can be done by plotting the functions of y in (s5.1) and (s5.5) and finding their crossing point. In our case of MBT, $j = 5/2$ for each Mn atom, $T_C = 25$ K. As the RKKY interaction is considered, reducing $\mathfrak{I}_{ij}$ will also lead to smaller λ and T_C as shown in (s5.3) and (s5.4), which finally results in a smaller M.

At $T = 10$ K, $M/M_s \approx 0.938$ as shown in Fig. S7(a). When $\mathfrak{I}_{ij}$ is reduced by 30 %, $M/M_s \approx 0.845$ (Fig. S7(b)), which means the demagnetization is about 1 -0.845/0.938 ≈ 10%.

The Van Vleck coupling involves excited states of valence electrons, which is mostly T_e-independent (*8*). Moreover, the superexchange interaction depends on how well the *p* and *d* orbitals overlap in covalent bonds, which will vary in response to thermal lattice expansion and vibrations (*53*) but can be neglected in the first 500 fs. Therefore, if the magnetism in the bulk of MBT is dominated by the Van Vleck or superexchange interactions, the initial fast demagnetization due to RKKY interactions will be much smaller in magnitude measured by the bulk-sensitive trMOKE experiments, as compared to the theoretical prediction above.

To extract the appropriate value for the initial demagnetization from trMOKE, we first obtain ~1% at 200 fs for the pump fluence of 20 μJ/cm^2 (Fig. S8). Moreover, we take into account the different pumping and probing depths in the trARPES and trMOKE experiments. We calculate the average absorbed energy density for each experiment by the following equation:

$$\langle D\rangle_{\mathrm{obs}}=\frac{\int_0^\infty dzF(1-R)e^{\frac{-z}{d_{\mathrm{pump}}}}\,e^{\frac{-z}{d_{\mathrm{probe}}}}}{\int_0^\infty dze^{\frac{-z}{d_{\mathrm{pump}}}}\int_0^\infty dz\,e^{\frac{-z}{d_{\mathrm{probe}}}}},\quad \text{(s5.6)}$$

where F is the pump fluence; R is the reflectance; d_{pump} and d_{probe} are the pumping and probing depths, respectively. Generally, d_{pump} and d_{probe} at specific wavelengths are obtained using the imaginary part of the refractive indices (*84*), except for that d_{probe} of the trARPES experiment is determined by the inelastic mean free path of the photoexcited electrons in solids (*85*). For trARPES, $R = 0.41$, $d_{\mathrm{pump}} \approx 20.9$ nm and $d_{\mathrm{probe}} \approx 4$ nm; while for trMOKE, $R = 0.52$, $d_{\mathrm{pump}} \approx 17.5$ nm and $d_{\mathrm{probe}} \approx 20.9$ nm. Thus, the ratio of the average absorbed energy densities is $\langle D\rangle_{\mathrm{obs}}^{\mathrm{trARPES}}\big/\langle D\rangle_{\mathrm{obs}}^{\mathrm{trMOKE}} \approx 1.9$. Based on this result, we estimate that the effective demagnetization magnitude in the trMOKE experiment is ~1.9 % for the same energy absorption as in the trARPES measurements.

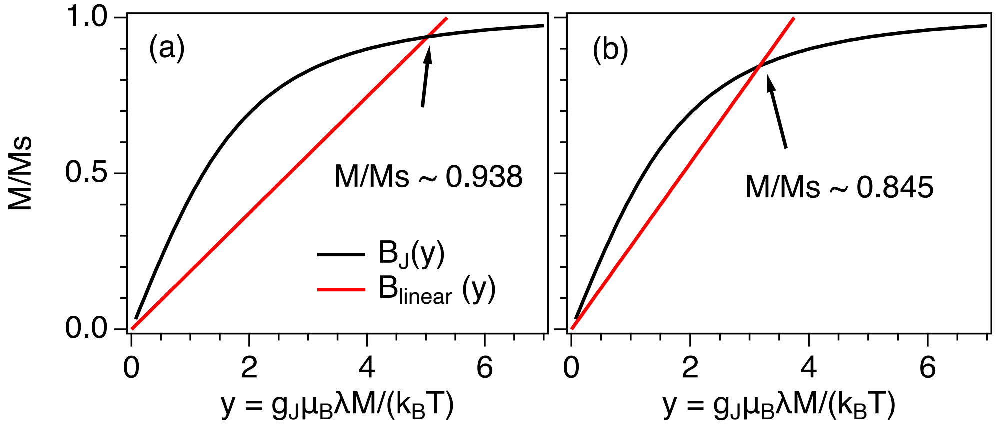

Fig. S7. The reduction of magnetization following the reduction of the RKKY coupling constant. (a) The original M/M_s value is graphically found to be 0.938. (b) 30% reduction of the RKKY strength leads to a new M/M_s value of 0.845.

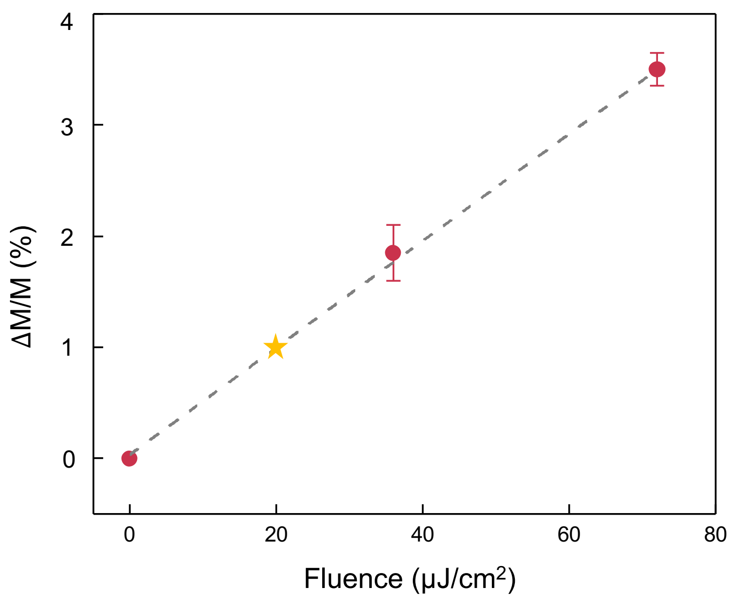

Fig. S8. Extrapolated demagnetization at 200 fs for the pump fluence of 20 μJ/cm^2 (yellow star) based on the linear dependence of the demagnetization on the incident pump fluences.

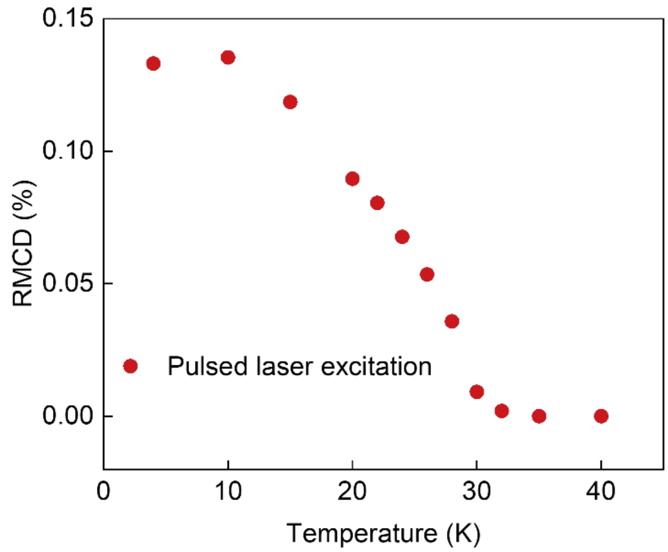

Fig. S9. The temperature-dependent RMCD was measured with a pulsed laser (1.9 eV) with the fluence ~ 60 μJ/cm^2, which is similar to the pump laser conditions. The observed magnetic transition temperature shows there is no substantial lattice heating due to the pump laser illumination. The transition temperature (~28 K) is slightly higher than what has been reported in the literature (~25 K) (*29*), which is attributed to the temperature difference between the cryostat sample heat plate and the sample surface.

6. Elliott-Yafet-Type Spin-Flip Model

We follow Koopmans *et al.* (*54*) for the Elliott-Yafet model, which is formulated by three coupled differential equations:

$$C_e(T_e)\frac{dT_e}{dt} = \nabla_z(\kappa\nabla_z T_e) + g_{ep}\left(T_p - T_e\right),$$
$$C_p\frac{dT_p}{dt} = \nabla_z(\kappa\nabla_z T_e) + g_{ep}\left(T_e - T_p\right), \qquad \text{(s6.1)}$$
$$\frac{dm}{dt} = Rm\frac{T_p}{T_C}(1 - m\coth(\frac{mT_C}{T_e})).$$

Here, κ is the electronic thermal conductivity, g_{ep} is the electron-phonon coupling constant, $m \equiv M/M_s$, T_C is the Curie temperature of the ferromagnet; C_e and C_p are the electronic and phononic heat capacities, respectively. R is defined as

$$R = \frac{8a_{sf}g_{ep}k_B T_C^2 V_{at}}{E_D^2\mu_{at}/\mu_B}, \qquad (s6.2)$$

where a_{sf} is phonon-induced spin flip probability; V_{at} is the atomic volume in the case of elemental magnets; E_D is the Debye energy; μ_{at} is the atomic magnetic moment; and μ_B is the Bohr magneton. We used T_e as obtained from Supplementary Text 1, T_p as obtained by the microscopic Boltzmann model in Supplementary Text 2, and the following selection of parameters for MBT based on Refs. (*31*, *54*). $a_{sf} = 0.06$, $g_{ep} = 0.27 \times 10^3$ $JK^{-1}m^{-3}fs^{-1}$, $V_{at} = 4/3\pi \times (1.6 \times 10^3)^3$ m^3 (volume of a Bi atom), $\mu_{at} = 0.05$ for a combined *p*-spin of Bi and Te, $E_D = k_B T_D \approx 100k_B$ (*31*, *55*). The resulted dynamics of magnetization is completely different from experimental data, as shown in Fig. S10. The magnetization quickly collapses to zero within the first 1 ps, and never recovers in the next 6 ps. The fundamental reason for this result is that the T_e we used reaches > 500 K near time zero, which is 20 times bigger than the magnetic transition temperature (25 K). In a traditional ferromagnetic metal, this transient electronic temperature would have led to a complete demagnetization, reflected by Fig. S10. However, in a *p-d* coupled system such as MBT, where the RKKY mechanism connects the *p*-electrons and the 3*d* moments, the high temperature of the *p*-electrons only has a small impact on the magnetization as seen in our experiment.

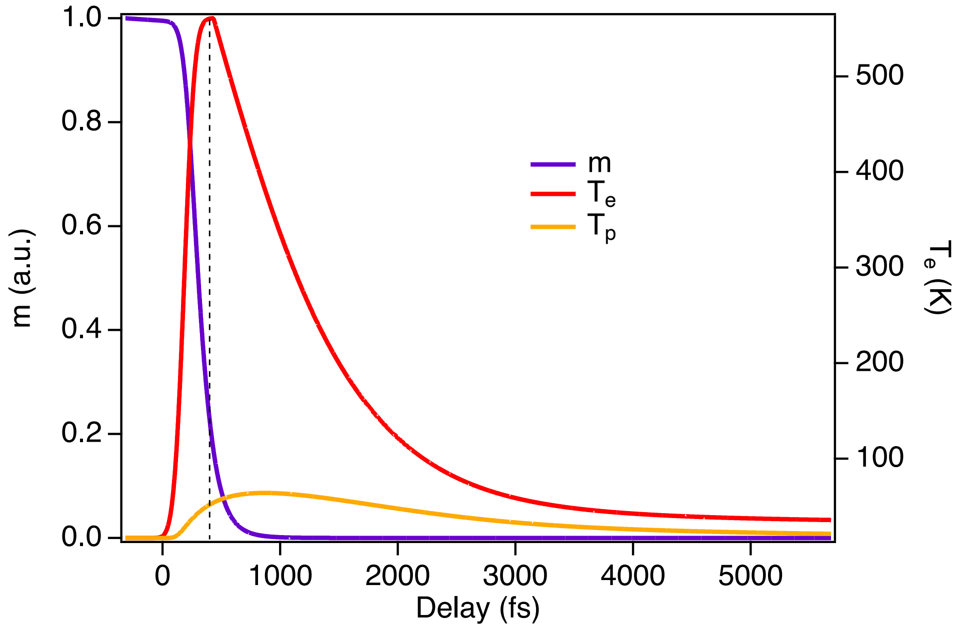

Fig. S10. Elliot-Yafet-type three-temperature model fails to capture the ultrafast demagnetization in MBT. The electronic temperature and phonon temperature are collected from fittings in Supplementary Texts 1 and 2.

7. Landau-Lifshitz-Gilbert (LLG) model

The LLG model starts with a Heisenberg-type Hamiltonian:

$$H = -\sum_{ij} J_{ij}\boldsymbol{S}_i \cdot \boldsymbol{S}_j - K\sum_i S_i^{z2} - J_{pd}\sum_i \boldsymbol{S}_i \cdot \boldsymbol{s}_i. \tag{s7.1}$$

This Hamiltonian is a more comprehensive Hamiltonian compared to Eqn. (1) in the main text. The exchange coupling constant (J_{ij}) here includes all coupling channels for two 3*d* spins (superexchange and others), while K is the single-ion anisotropy coefficient which breaks the continuous symmetry in 2D, making ferromagnetic ground state possible (avoiding the Wigner-Mermin theorem). S_i^z is the z-component of $\boldsymbol{S}_i$, and J_{pd} is the intra-atomic exchange coupling constant for the *d* spin and *p* spin in one atom. From this Hamiltonian, the effective field in the LLG equation can be calculated:

$$\boldsymbol{H}_{eff}^i = -\frac{\partial H}{\partial \boldsymbol{S}_i} + \boldsymbol{H}_{noise}^i. \tag{s7.2}$$

The general LLG equation is:

$$\frac{d\boldsymbol{S}_i}{dt} = -\frac{\gamma}{1+\lambda^2}\left[\boldsymbol{S}_i \times \boldsymbol{H}_{eff}^i + \lambda \boldsymbol{S}_i \times \left(\boldsymbol{S}_i \times \boldsymbol{H}_{eff}^i\right)\right] \tag{s7.3}$$

for both *d*- and *p*-spins, where, γ is the gyromagnetic ratio and λ is the Gilbert damping parameter. In fact, the superexchange is barely affected on our time scale (<500 fs) due to the slow thermal responses of the lattice. The first term in (s7.1) rather contributes a constant in the effective field written in (s7.2), and the dynamics is mainly contributed by the last term with J_{pd}. In that case we can consider the effective Hamiltonian for the ultrafast dynamics as:

$$H' = -J_{pd}\sum_i \boldsymbol{S}_i \cdot \boldsymbol{s}_i. \tag{s7.4}$$

This Hamiltonian is in fact the Kondo lattice Hamiltonian we discussed in Supplementary Text 3. Since both models start with the same Hamiltonian, fundamentally they are equivalent up to the treatment of the effective fields in the LLG model and the scaling renormalization in the RKKY model.

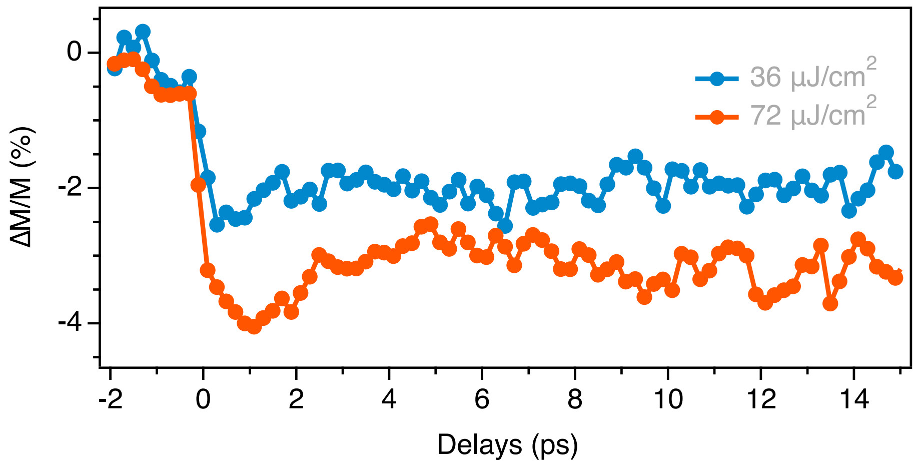

Fig. S11. trMOKE data for a longer time scale for both 36 and 72 μJ/cm² IR pumping fluences

REFERENCES AND NOTES

1. C.-Z. Chang, J. Zhang, X. Feng, J. Shen, Z. Zhang, M. Guo, K. Li, Y. Ou, P. Wei, L. L. Wang, Z. Q. Ji, Y. Feng, S. Ji, X. Chen, J. Jia, X. Dai, Z. Fang, S. C. Zhang, K. He, Y. Wang, L. Lu, X. C. Ma, Q. K. Xue, Experimental observation of the quantum anomalous hall effect in a magnetic topological insulator. *Science* **340**, 167–170 (2013).

2. Y. Deng, Y. Yu, M. Z. Shi, Z. Guo, Z. Xu, J. Wang, X. H. Chen, Y. Zhang, Quantum anomalous Hall effect in intrinsic magnetic topological insulator $MnBi_2Te_4$. *Science* **367**, 895–900 (2020).

3. X.-L. Qi, T. L. Hughes, S.-C. Zhang, Topological field theory of time-reversal invariant insulators. *Phys. Rev. B* **78**, 195424 (2008).

4. F. Wilczek, Two applications of axion electrodynamics. *Phys. Rev. Lett.* **58**, 1799–1802 (1987).

5. C. Liu, Y. Wang, H. Li, Y. Wu, Y. Li, J. Li, K. He, Y. Xu, J. Zhang, Y. Wang, Robust axion insulator and Chern insulator phases in a two-dimensional antiferromagnetic topological insulator. *Nat. Mater.* **19**, 522–527 (2020).

6. C.-Z. Chang, C.-X. Liu, A. H. MacDonald, Colloquium: Quantum anomalous Hall effect. *Rev. Mod. Phys.* **95**, 011002 (2023).

7. C. Śliwa, C. Autieri, J. A. Majewski, T. Dietl, Superexchange dominates in magnetic topological insulators. *Phys. Rev. B* **104**, L220404 (2021).

8. J. H. Van Vleck, On dielectric constants and magnetic susceptibilities in the new quantum mechanics part III—Application to dia- and paramagnetism. *Phys. Rev.* **31**, 587–613 (1928).

9. R. Yu, W. Zhang, H. J. Zhang, S. C. Zhang, X. Dai, Z. Fang, Quantized anomalous Hall effect in magnetic topological insulators. *Science* **329**, 61–64 (2010).

10. R. Watanabe, R. Yoshimi, M. Kawamura, M. Mogi, A. Tsukazaki, X. Z. Yu, K. Nakajima, K. S. Takahashi, M. Kawasaki, Y. Tokura, Quantum anomalous Hall effect driven by magnetic proximity coupling in all-telluride based heterostructure. *Appl. Phys. Lett.* **115**, 102403 (2019).

11. Q. Liu, C. X. Liu, C. Xu, X. L. Qi, S. C. Zhang, Magnetic impurities on the surface of a topological insulator. *Phys. Rev. Lett.* **102**, 156603 (2009).

12. J. Wang, B. Lian, S.-C. Zhang, Quantum anomalous Hall effect in magnetic topological insulators. *Phys. Scr.* **T164**, 014003 (2015).

13. D. Pesin, A. H. MacDonald, Spintronics and pseudospintronics in graphene and topological insulators. *Nat. Mater.* **11**, 409–416 (2012).

14. D. K. Efimkin, V. Galitski, Self-consistent theory of ferromagnetism on the surface of a topological insulator. *Phys. Rev. B* **89**, 115431 (2014).

15. D. A. Abanin, D. A. Pesin, Ordering of magnetic impurities and tunable electronic properties of topological insulators. *Phys. Rev. Lett.* **106**, 136802 (2011).

16. J.-J. Zhu, D. X. Yao, S. C. Zhang, K. Chang, Electrically controllable surface magnetism on the surface of topological insulators. *Phys. Rev. Lett.* **106**, 097201 (2011).

17. R. R. Biswas, A. V. Balatsky, Impurity-induced states on the surface of three-dimensional topological insulators. *Phys. Rev. B* **81**, 233405 (2010).

18. J. G. Checkelsky, J. Ye, Y. Onose, Y. Iwasa, Y. Tokura, Dirac-fermion-mediated ferromagnetism in a topological insulator. *Nat. Phys.* **8**, 729–733 (2012).

19. P. Sessi, F. Reis, T. Bathon, K. A. Kokh, O. E. Tereshchenko, M. Bode, Signatures of Dirac fermion-mediated magnetic order. *Nat. Commun.* **5**, 5349 (2014).

20. X. Kou, L. He, M. Lang, Y. Fan, K. Wong, Y. Jiang, T. Nie, W. Jiang, P. Upadhyaya, Z. Xing, Y. Wang, F. Xiu, R. N. Schwartz, K. L. Wang, Manipulating surface-related ferromagnetism in modulation-doped topological insulators. *Nano Lett.* **13**, 4587–4593 (2013).

21. W. Wang, Y. Ou, C. Liu, Y. Wang, K. He, Q. K. Xue, W. Wu, Direct evidence of ferromagnetism in a quantum anomalous Hall system. *Nat. Phys.* **14**, 791–795 (2018).

22. W. Lee, S. Fernandez-Mulligan, H. Tan, C. Yan, Y. Guan, S. H. Lee, R. Mei, C. Liu, B. Yan, Z. Mao, S. Yang, Layer-by-layer disentanglement of Bloch states. *Nat. Phys.* **19**, 950–955 (2023).

23. C. Yan, S. Fernandez-Mulligan, R. Mei, S. H. Lee, N. Protic, R. Fukumori, B. Yan, C. Liu, Z. Mao, S. Yang, Origins of electronic bands in the antiferromagnetic topological insulator $MnBi_2Te_4$. *Phys. Rev. B* **104**, L041102 (2021).

24. D. Nevola, H. X. Li, J. Q. Yan, R. G. Moore, H. N. Lee, H. Miao, P. D. Johnson, Coexistence of surface ferromagnetism and a gapless topological state in $MnBi_2Te_4$. *Phys. Rev. Lett.* **125**, 117205 (2020).

25. Y.-J. Hao, P. Liu, Y. Feng, X. M. Ma, E. F. Schwier, M. Arita, S. Kumar, C. Hu, R.’. Lu, M. Zeng, Y. Wang, Z. Hao, H. Y. Sun, K. Zhang, J. Mei, N. Ni, L. Wu, K. Shimada, C. Chen, Q. Liu, C. Liu, Gapless surface Dirac cone in antiferromagnetic topological insulator $MnBi_2Te_4$. *Phys. Rev. X* **9**, 041038 (2019).

26. Y. J. Chen, L. X. Xu, J. H. Li, Y. W. Li, H. Y. Wang, C. F. Zhang, H. Li, Y. Wu, A. J. Liang, C. Chen, S. W. Jung, C. Cacho, Y. H. Mao, S. Liu, M. X. Wang, Y. F. Guo, Y. Xu, Z. K. Liu, L. X. Yang, Y. L. Chen, Topological electronic structure and its temperature evolution in antiferromagnetic topological insulator $MnBi_2Te_4$. *Phys. Rev. X* **9**, 041040 (2019).

27. M. M. Otrokov, I. I. Klimovskikh, H. Bentmann, D. Estyunin, A. Zeugner, Z. S. Aliev, S. Gaß, A. U. B. Wolter, A. V. Koroleva, A. M. Shikin, M. Blanco-Rey, M. Hoffmann, I. P. Rusinov, A. Y. Vyazovskaya, S. V. Eremeev, Y. M. Koroteev, V. M. Kuznetsov, F. Freyse, J. Sánchez-Barriga, I. R. Amiraslanov, M. B. Babanly, N. T. Mamedov, N. A. Abdullayev, V. N. Zverev, A. Alfonsov, V. Kataev, B. Büchner, E. F. Schwier, S. Kumar, A. Kimura, L. Petaccia, G. di Santo, R. C. Vidal, S. Schatz, K. Kißner, M. Ünzelmann, C. H. Min, S. Moser, T. R. F. Peixoto, F. Reinert, A. Ernst, P. M. Echenique, A. Isaeva, E. V. Chulkov, Prediction and observation of an antiferromagnetic topological insulator. *Nature* **576**, 416–422 (2019).

28. Y.-F. Zhao, L. J. Zhou, F. Wang, G. Wang, T. Song, D. Ovchinnikov, H. Yi, R. Mei, K. Wang, M. H. W. Chan, C. X. Liu, X. Xu, C. Z. Chang, Even-odd layer-dependent anomalous Hall effect in topological magnet $MnBi_2Te_4$ thin films. *Nano Lett.* **21**, 7691–7698 (2021).

29. S. Yang, X. Xu, Y. Zhu, R. Niu, C. Xu, Y. Peng, X. Cheng, X. Jia, Y. Huang, X. Xu, J. Lu, Y. Ye, Odd-even layer-number effect and layer-dependent magnetic phase diagrams in $MnBi_2Te_4$. *Phys. Rev. X* **11**, 011003 (2021).

30. P. E. Majchrzak, Y. Liu, K. Volckaert, D. Biswas, C. Sahoo, D. Puntel, W. Bronsch, M. Tuniz, F. Cilento, X. C. Pan, Q. Liu, Y. P. Chen, S. Ulstrup, Van der Waals engineering of ultrafast carrier dynamics in magnetic heterostructures. *Nano Lett.* **23**, 414–421 (2023).

31. H. Padmanabhan, V. A. Stoica, P. K. Kim, M. Poore, T. Yang, X. Shen, A. H. Reid, M. F. Lin, S. Park, J. Yang, H. (H.) Wang, N. Z. Koocher, D. Puggioni, A. B. Georgescu, L. Min, S. H. Lee, Z. Mao, J. M. Rondinelli, A. M. Lindenberg, L. Q. Chen, X. Wang, R. D. Averitt, J. W. Freeland, V. Gopalan, Large exchange coupling between localized spins and topological bands in $MnBi_2Te_4$. *Adv. Mater.* **34**, e2202841 (2022).

32. D. Ovchinnikov, X. Huang, Z. Lin, Z. Fei, J. Cai, T. Song, M. He, Q. Jiang, C. Wang, H. Li, Y. Wang, Y. Wu, D. Xiao, J. H. Chu, J. Yan, C. Z. Chang, Y. T. Cui, X. Xu, Intertwined topological and magnetic orders in atomically thin chern insulator $MnBi_2Te_4$. *Nano Lett.* **21**, 2544–2550 (2021).

33. M. Wu, Z. Li, T. Cao, S. G. Louie, Physical origin of giant excitonic and magneto-optical responses in two-dimensional ferromagnetic insulators. *Nat. Comm.* **10**, 2371 (2019).

34. J. Ahn, S.-Y. Xu, A. Vishwanath, Theory of optical axion electrodynamics and application to the Kerr effect in topological antiferromagnets. *Nat. Comm.* **13**, 7615 (2022).

35. J. Cai, D. Ovchinnikov, Z. Fei, M. He, T. Song, Z. Lin, C. Wang, D. Cobden, J. H. Chu, Y. T. Cui, C. Z. Chang, D. Xiao, J. Yan, X. Xu, Electric control of a canted-antiferromagnetic Chern insulator. *Nat. Comm.* **13**, 1668 (2022).

36. M. A. Ruderman, C. Kittel, Indirect exchange coupling of nuclear magnetic moments by conduction electrons. *Phys. Rev.* **96**, 99–102 (1954).

37. T. Kasuya, A theory of metallic ferro- and antiferromagnetism on Zener’s model. *Prog. Theor. Phys.* **16**, 45–57 (1956).

38. K. Yosida, Magnetic properties of Cu-Mn alloys. *Phys. Rev.* **106**, 893–898 (1957).

39. D. A. Estyunin, I. I. Klimovskikh, A. M. Shikin, E. F. Schwier, M. M. Otrokov, A. Kimura, S. Kumar, S. O. Filnov, Z. S. Aliev, M. B. Babanly, E. V. Chulkov, Signatures of temperature driven antiferromagnetic transition in the electronic structure of topological insulator $MnBi_2Te_4$. *APL Mat.* **8**, 021105 (2020).

40. R. C. Vidal, H. Bentmann, T. R. F. Peixoto, A. Zeugner, S. Moser, C.-H. Min, S. Schatz, K. Kißner, M. Ünzelmann, C. I. Fornari, H. B. Vasili, M. Valvidares, K. Sakamoto, D. Mondal, J. Fujii, I. Vobornik, S. Jung, C. Cacho, T. K. Kim, R. J. Koch, C. Jozwiak, A. Bostwick, J. D. Denlinger, E. Rotenberg, J. Buck, M. Hoesch, F. Diekmann, S. Rohlf, M. Kalläne, K. Rossnagel, M. M. Otrokov, E. V. Chulkov, M. Ruck, A. Isaeva, F. Reinert, Surface states and Rashba-type spin polarization in antiferromagnetic $MnBi_2Te_4$(0001). *Phys. Rev. B* **100**, 121104 (2019).

41. J. H. Van Vleck, Note on the Interactions between the Spins of Magnetic Ions or Nuclei in Metals. *Rev. Mod. Phys.* **34**, 681–686 (1962).

42. B. Simons, A. Altland, *Condensed Matter Field Theory* (Cambridge Univ. Press, ed. 3, 2010).

43. P. Coleman, *Introduction to Many-Body Physics* (Cambridge Univ. Press, 2015).

44. J. Kondo, Resistance minimum in dilute magnetic alloys. *Prog. Theor. Phys.* **32**, 37–49 (1964).

45. P. Coleman, Heavy fermions and the Kondo lattice: A 21st century perspective. arXiv:1509.05769 (2015).

46. P. W. Anderson, A poor man's derivation of scaling laws for the Kondo problem. *J. Phys. C: Solid State Phys.* **3**, 2436 (1970).

47. K. Sato, L. Bergqvist, J. Kudrnovský, P. H. Dederichs, O. Eriksson, I. Turek, B. Sanyal, G. Bouzerar, H. Katayama-Yoshida, V. A. Dinh, T. Fukushima, H. Kizaki, R. Zeller, First-principles theory of dilute magnetic semiconductors. *Rev. Mod. Phys.* **82**, 1633–1690 (2010).

48. Z. Fei, B. Huang, P. Malinowski, W. Wang, T. Song, J. Sanchez, W. Yao, D. Xiao, X. Zhu, A. F. May, W. Wu, D. H. Cobden, J. H. Chu, X. Xu, Two-dimensional itinerant ferromagnetism in atomically thin Fe_3GeTe_2. *Nat. Mater* **17**, 778–782 (2018).

49. M. Khela, M. Dąbrowski, S. Khan, P. S. Keatley, I. Verzhbitskiy, G. Eda, R. J. Hicken, H. Kurebayashi, E. J. G. Santos, Laser-induced topological spin switching in a 2D van der Waals magnet. *Nat. Comm.* **14**, 1378 (2023).

50. K. Yamagami, Y. Fujisawa, B. Driesen, C. H. Hsu, K. Kawaguchi, H. Tanaka, T. Kondo, Y. Zhang, H. Wadati, K. Araki, T. Takeda, Y. Takeda, T. Muro, F. C. Chuang, Y. Niimi, K. Kuroda, M. Kobayashi, Y. Okada, Itinerant ferromagnetism mediated by giant spin polarization of the metallic ligand band in the van der Waals magnet Fe_5GeTe_2. *Phys. Rev. B* **103**, L060403 (2021).

51. M. Strungaru, M. Augustin, E. J. G. Santos, Ultrafast laser-driven topological spin textures on a 2D magnet. *NPJ Comput. Mater.* **8**, 169 (2022).

52. K. Mæland, H. I. Røst, J. W. Wells, A. Sudbø, Electron-magnon coupling and quasiparticle lifetimes on the surface of a topological insulator. *Phys. Rev. B* **104**, 125125 (2021).

53. S. K. Hoffmann, W. Hilczer, J. Goslar, Weak long-distance superexchange interaction and its temperature variations in copper(II) compounds studied by single crystal EPR. *Appl. Magn. Reson.* **7**, 289–321 (1994).

54. B. Koopmans, G. Malinowski, F. Dalla Longa, D. Steiauf, M. Fähnle, T. Roth, M. Cinchetti, M. Aeschlimann, Explaining the paradoxical diversity of ultrafast laser-induced demagnetization. *Nat. Mat.* **9**, 259–265 (2010).

55. J.-Q. Yan, Y. H. Liu, D. S. Parker, Y. Wu, A. A. Aczel, M. Matsuda, M. A. McGuire, B. C. Sales, A-type antiferromagnetic order in $MnBi_4Te_7$ and $MnBi_6Te_{10}$ single crystals. *Phys. Rev. Mat.* **4**, 054202 (2020).

56. J. Sitnicka, K. Park, P. Skupiński, K. Grasza, A. Reszka, K. Sobczak, J. Borysiuk, Z. Adamus, M. Tokarczyk, A. Avdonin, I. Fedorchenko, I. Abaloszewa, S. Turczyniak-Surdacka, N. Olszowska, J. Kołodziej, B. J. Kowalski, H. Deng, M. Konczykowski, L. Krusin-Elbaum, A. Wołoś, Systemic

consequences of disorder in magnetically self-organized topological $MnBi_2Te_4/(Bi_2Te_3)_n$ superlattices. *2D Mater.* **9**, 015026 (2022).

57. H. Tan, B. Yan, Distinct magnetic gaps between antiferromagnetic and ferromagnetic orders driven by surface defects in the topological magnet $MnBi_2Te_4$. *Phys. Rev. Lett.* **130**, 126702 (2023).

58. R. Mei, Y.-F. Zhao, C. Wang, Y. Ren, D. Xiao, C.-Z. Chang, C.-X. Liu, Electrically controlled anomalous hall effect and orbital magnetization in topological magnet $MnBi_2Te_4$. *Phys. Rev. Lett.* **132**, 066604 (2024)

59. M. Bernardi, C. Ataca, M. Palummo, J. C. Grossman, Optical and electronic properties of two-dimensional layered materials. *Nanophotonics* **6**, 479–493 (2017).

60. E. Carpene, E. Mancini, C. Dallera, M. Brenna, E. Puppin, S. de Silvestri, Dynamics of electron-magnon interaction and ultrafast demagnetization in thin iron films. *Phys. Rev. B* **78**, 174422 (2008).

61. A. L. Chekhov, Y. Behovits, J. J. F. Heitz, C. Denker, D. A. Reiss, M. Wolf, M. Weinelt, P. W. Brouwer, M. Münzenberg, T. Kampfrath, Ultrafast demagnetization of iron induced by optical versus terahertz pulses. *Phys. Rev. X* **11**, 041055 (2021).

62. A. Eschenlohr, M. Battiato, P. Maldonado, N. Pontius, T. Kachel, K. Holldack, R. Mitzner, A. Föhlisch, P. M. Oppeneer, C. Stamm, Ultrafast spin transport as key to femtosecond demagnetization. *Nat. Mater* **12**, 332–336 (2013).

63. L. Guidoni, E. Beaurepaire, J.-Y. Bigot, Magneto-optics in the ultrafast regime: Thermalization of spin populations in ferromagnetic films. *Phys. Rev. Lett.* **89**, 017401 (2002).

64. A. V. Kimel, R. V. Pisarev, J. Hohlfeld, T. Rasing, Ultrafast quenching of the antiferromagnetic order in $FeBO_3$: Direct optical probing of the phonon-magnon coupling. *Phys. Rev. Lett.* **89**, 287401 (2002).

65. T. Kise, T. Ogasawara, M. Ashida, Y. Tomioka, Y. Tokura, M. Kuwata-Gonokami, Ultrafast spin dynamics and critical behavior in half-metallic ferromagnet: Sr_2FeMoO_6. *Phys. Rev. Lett.* **85**, 1986–1989 (2000).

66. K. Mishra, R. M. Rowan-Robinson, A. Ciuciulkaite, C. S. Davies, A. Dmitriev, V. Kapaklis, A. V. Kimel, A. Kirilyuk, Ultrafast demagnetization control in magnetophotonic surface crystals. *Nano Lett.* **22**, 9773–9780 (2022).

67. C. D. Stanciu, A. Tsukamoto, A. V. Kimel, F. Hansteen, A. Kirilyuk, A. Itoh, T. Rasing, Subpicosecond magnetization reversal across ferrimagnetic compensation points. *Phys. Rev. Lett.* **99**, 217204 (2007).

68. R. Takahashi, Y. Tani, H. Abe, M. Yamasaki, I. Suzuki, D. Kan, Y. Shimakawa, H. Wadati, Ultrafast demagnetization in $NiCo_2O_4$ thin films probed by time-resolved microscopy. *Appl. Phys. Lett.* **119**, 102404 (2021).

69. P. Tengdin, W. You, C. Chen, X. Shi, D. Zusin, Y. Zhang, C. Gentry, A. Blonsky, M. Keller, P. M. Oppeneer, H. C. Kapteyn, Z. Tao, M. M. Murnane, Critical behavior within 20 fs drives the out-of-equilibrium laser-induced magnetic phase transition in nickel. *Sci. Adv.* **4**, eaap9744 (2018).

70. J. Wang, C. Sun, J. Kono, A. Oiwa, H. Munekata, Ł. Cywiński, L. J. Sham, Ultrafast quenching of ferromagnetism in InMnAs induced by intense laser irradiation. *Phys. Rev. Lett.* **95**, 167401 (2005).

71. M. Wietstruk, A. Melnikov, C. Stamm, T. Kachel, N. Pontius, M. Sultan, C. Gahl, M. Weinelt, H. A. Dürr, U. Bovensiepen, Hot-electron-driven enhancement of spin-lattice coupling in Gd and Tb *4f* ferromagnets observed by femtosecond X-ray magnetic circular dichroism. *Phys. Rev. Lett.* **106**, 127401 (2011).

72. J.-X. Qiu, C. Tzschaschel, J. Ahn, A. Gao, H. Li, X. Y. Zhang, B. Ghosh, C. Hu, Y. X. Wang, Y. F. Liu, D. Bérubé, T. Dinh, Z. Gong, S. W. Lien, S. C. Ho, B. Singh, K. Watanabe, T. Taniguchi, D. C. Bell, H. Z. Lu, A. Bansil, H. Lin, T. R. Chang, B. B. Zhou, Q. Ma, A. Vishwanath, N. Ni, S. Y. Xu, Axion optical induction of antiferromagnetic order. *Nat. Mater.* **22**, 583–590 (2023).

73. K. Yasuda, M. Mogi, R. Yoshimi, A. Tsukazaki, K. S. Takahashi, M. Kawasaki, F. Kagawa, Y. Tokura, Quantized chiral edge conduction on domain walls of a magnetic topological insulator. *Science* **358**, 1311–1314 (2017).

74. O. Breunig, Y. Ando, Opportunities in topological insulator devices. *Nat. Rev. Phys.* **4**, 184–193 (2022).

75. S. H. Lee, D. Graf, L. Min, Y. Zhu, H. Yi, S. Ciocys, Y. Wang, E. S. Choi, R. Basnet, A. Fereidouni, A. Wegner, Y. F. Zhao, K. Verlinde, J. He, R. Redwing, V. Gopalan, H. O. H. Churchill, A. Lanzara, N. Samarth, C. Z. Chang, J. Hu, Z. Q. Mao, Evidence for a magnetic-field-induced ideal type-II Weyl state in antiferromagnetic topological insulator $Mn(Bi_{1-x}Sb_x)_2Te_4$. *Phys. Rev. X* **11**, 031032 (2021).

76. C. Yan, E. Green, R. Fukumori, N. Protic, S. H. Lee, S. Fernandez-Mulligan, R. Raja, R. Erdakos, Z. Mao, S. Yang, An integrated quantum material testbed with multi-resolution photoemission spectroscopy. *Rev. Sci. Instrum.* **92**, 113907 (2021).

77. S. Harris, *An Introduction to the Theory of the Boltzmann Equation (Dover Books on Physics)* (Dover Publications, 2004).

78. G. Grimvall, *The Electron-Phonon Interaction in Metals*, Series of Monographs on Selected Topics in Solid State Physics (North-Holland Publishing Co., 1981).

79. P. B. Allen, Theory of thermal relaxation of electrons in metals. *Phys. Rev. Lett.* **59**, 1460–1463 (1987).

80. J. Ning, Y. Zhu, J. Kidd, Y. Guan, Y. Wang, Z. Mao, J. Sun, Subtle metastability of the layered magnetic topological insulator $MnBi_2Te_4$ from weak interactions. *NPJ Comput. Mater.* **6**, 157 (2020).

81. B. Li, J. Q. Yan, D. M. Pajerowski, E. Gordon, A. M. Nedić, Y. Sizyuk, L. Ke, P. P. Orth, D. Vaknin, R. J. McQueeney, Competing magnetic interactions in the antiferromagnetic topological insulator $MnBi_2Te_4$. *Phys. Rev. Lett.* **124**, 167204 (2020).

82. J. A. Sobota, S. Yang, J. G. Analytis, Y. L. Chen, I. R. Fisher, P. S. Kirchmann, Z. X. Shen, Ultrafast optical excitation of a persistent surface-state population in the topological insulator Bi_2Se_3. *Phys. Rev. Lett.* **108**, 117403 (2012).

83. S. Blundell, *Magnetism in Condensed Matter*, Oxford Master Series in Condensed Matter Physics (Oxford Univ. Press, 2014).

84. Z. A. Jahangirli, E. H. Alizade, Z. S. Aliev, M. M. Otrokov, N. A. Ismayilova, S. N. Mammadov, I. R. Amiraslanov, N. T. Mamedov, G. S. Orudjev, M. B. Babanly, A. M. Shikin, E. V. Chulkov, Electronic structure and dielectric function of Mn-Bi-Te layered compounds. *J. Vac. Sci. Technol. B Nanotechnol. Microelectron.* **37**, 062910 (2019).

85. M. P. Seah, W. A. Dench, Quantitative electron spectroscopy of surfaces: A standard data base for electron inelastic mean free paths in solids. *Surf. Interface Anal.* **1**, 2–11 (1979).